Anisotropic response of Ti-6Al-4V alloy fabricated by 3D printing selective laser melting

L.Y. Chen[a], J.C. Huang[a],[*], C.H. Lin[b], C.T. Pan[b], S.Y. Chen[a], T.L. Yang[b], D.Y. Lin[c], H.K. Lin[d], J.S.C. Jang[e]

[a] Department of Materials and Optoelectronic Science, National Sun Yat-Sen University, Kaohsiung 804, Taiwan
[b] Department of Mechanical and Electro-Mechanical Engineering, National Sun Yat-Sen University, Kaohsiung 80424, Taiwan
[c] Industrial Technology Research Institute, Hsinchu, 31040 Taiwan, ROC
[d] Graduate Institute of Materials Engineering, National Pingtung University of Science and Technology, Pingtung 91201, Taiwan
[e] Institute of Materials Science and Engineering, Department of Mechanical Engineering, National Central University Taoyuan 32001, Taiwan

ARTICLE INFO

ABSTRACT

The 3D printed bulk samples fabricated by selective laser melting (SLM) of the additive manufacturing technique are usually considered to be 3D isotropic in microstructures and mechanical responses. This study systematically investigates the anisotropic responses in terms of hardness and electrochemical resistance for the X-, Y- and Z-planes of the SLM Ti-6Al-4V bulk samples fabricated with the zigzag laser path strategy. Results show that all SLM planes exhibit no significant difference in Young's modulus compared to the mechanically rolled plate. However, the X-plane, referred to the cross-sectional plane perpendicular to the laser moving direction, is found ~20% lower hardness and the lowest corrosion resistance compared to the Y- and Z-planes. The underlying reasoning is researched and discussed. The microstructure observations indicate that artifact holes are induced in the X-plane due to un-uniform laser intensity distribution between two neighboring printing lines. Alternatively, the Y- and Z-planes exhibit dense morphology due to multiple heating while zigzag scanning. Experimental results also indicate that the SLM materials exhibit higher corrosion resistance than the commercial rolled materials.

1. Introduction

Among various additive manufacturing (3D printing) techniques, selective laser melting (SLM) and selective laser sintering (SLS) for metallic powders are frequently adopted recently. The only major difference between SLM and SLS is the laser power in use. The SLM products can have excellent mechanical properties, equivalent to or even superior to those of the cast counterparts. Additionally, the SLM products can be prepared in complicated final shape, providing high application potential [1].

Titanium (Ti) alloys have higher specific strength, stronger resistance to creep and better corrosion resistance. Nowadays, Ti and its alloys are becoming more and more important in the material field, and usually being used in the aerospace field, biomaterial field, and chemical field [2]. Among all Ti alloys for biomedical uses, Ti-6Al-4V alloys account for 70–80% usage. It is the most common Ti alloy. The Young's modulus of Ti-6Al-4V (~120 GPa) is much lower than that of stainless steel AISI 316 L (~200 GPa) or Co-Cr-Mo alloys (~230 GPa). Especially the porous or foam structured Ti-6Al-4V has shown its

capability to avoid the stress shielding effect which might cause bone osteoporosis and induce nearby bone fracture [3]. The lower density of Ti-6Al-4V (4.43 g/cm^3) can also be effectively reduced to the weight for the implants in comparison with stainless steel and Co-Cr-Mo alloys. Alternatively, Ti-6Al-4V is easy to oxidize to form a compact oxide layer, TiO_2 [4], enhancing the corrosion resistance and revealing the excellent biocompatibility. Currently, Ti-6Al-4V appears to be one of the most popular biomedical alloy systems for additive manufacturing SLM.

The products manufactured by SLM tend to have a unique structure of column grain [5]. So far, there have been various kinds of metallic materials fabricated by SLM, including titanium alloys [6], stainless steel [7] and cobalt-chromium alloys [8], all have high potential for biomedical applications. However, this structure is unusual for the products manufactured through conventional cast or wrought methods. Obviously, the properties and microstructures of SLM produced materials could vary in different production planes due to the line- and layer-wise building (X-, Y-, Z-plane, as defined in Fig. 1). The elongated columnar grains appear more or less along the building
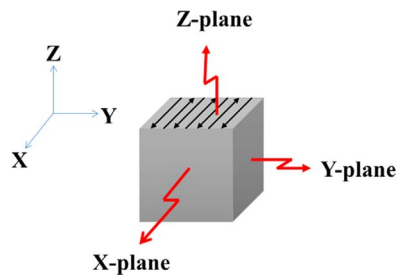
Fig. 1. The schematic diagram of SLM processed samples with X-plane, Y-plane and Z-plane. For simplicity, the plane perpendicular to the X-axis is termed as the X-plane. The substrate is located on the bottom side of this SLM solid sample. The laser scans back and forth on the Z-plane (and perpendicular to the X-plane), and the SLM sample accumulatively grows from the bottom to the top along the Z direction.

direction, but not necessary perfectly pointing to the Z vertical direction, sometimes can be slightly inclined [9,10]. Therefore, the directional microstructures in different planes can result in anisotropic material properties, such as ductility, toughness, fatigue strength, notch toughness and electro conduction. This study aims to explore the anisotropic characteristics for SLM fabricated Ti-6Al-4V bulk materials. The physical and chemical properties in terms of the mechanical properties, the electrochemical (EC) responses in simulated body fluid (SBF), i.e., their bio-corrosion resistance ability are investigated and compared with commercial rolled bulk materials.

2. Materials and methods

The Ti-6Al-4V powders (sphericity~1) fabricated by EOS Corp, Ltd, were adopted in this study. For comparison, a rolled commercial Ti-6Al-4V plate, 3 mm in thickness, was examined parallel as reference. The latter plate samples were polished by sandpaper (P800, P1000, P2000, and P4000 in sequence) and 3 μm Al_2O_3 powders.

The AM SLM printed solid (not porous) samples were fabricated by EOS M280, the SLM processing machine. The setting parameters included the laser power of 150–190 W, and scanning speed of 500–1250 mm/s in the continuous wavelength mode. The scanning strategy is the zigzag manner. By actual measurements, the laser spot size was about 70 μm, overlapping between two laser scanning paths was about 40 μm. The scanning spot area is about 3.8×10^{-5} cm^2, resulting in a scanning power density about 4×10^6 W/cm^2.

The crystal structure of SLM solid samples, from the X-, Y- and Z-planes, as well as the reference rolled plate, were characterized by SIEMENS D8000 X-ray diffractometer with a monochromatic Cu-K_α radiation (λ=0.15406 nm), equipped with a 0.02 mm graphite monochromator. The diffraction angle (2θ) covered from 30° to 80° with a scanning rate of 0.05° for every 4 seconds. Then, the microstructure and sample composition were characterized using the JEOL ISM-6330 TF scanning electron microscope (SEM) with energy dispersive X-ray spectrometer (EDS). The operating voltage, probe current and deriving time during the data collection were configured at 10 kV, 1×10^{-10} A, and 60 s, respectively. The resulting oxide layers were characterized by X-ray photoelectron spectroscopy (XPS).

Next, the mechanical properties and EC responses of the SLM samples along their X-, Y- and Z-planes were extracted by the MTS XP nanoindentation system and commercial electrochemical analyzer (CHI 614D, CHI instruments Inc., USA), respectively. The MTS XP nanoindentation system can measure the hardness and Young's modulus via the continuous stiffness measurement (CSM) mode [11]. The indented depth of this study is controlled around 3000 nm and the Poisson ratio is set to be 0.32.

The electrochemical properties of the SLM samples along their X-, Y- and Z-planes were immersed in the simulating body fluid (SBF) at 310 K, and the culture medium was evaluated using a commercial electrochemical analyzer. There were three testing models in the

current electrochemical experiment processes: the open circuit potential (OCP) curves, polarization Tafel curves, and A.C. electrochemical impedance spectra (EIS) impedance. Before the potentiodynamic polarization measurements, all the samples were shown that all of them are stable in SBF for 12,500 s with the criterion of the variation for the open circuit potential (OCP) less than 0.4 mV every 5 minutes. The potential scans are started from the value of OCP minus −0.2 to +2.0 V with a 0.33 mV/s scanning rate. Finally, the AC impedance test is carried out with an amplitude if 10 mV in open-circuit and the frequency range is 10^{-2} to 10^4 Hz. Additionally, the SBF uses in this study was the Hank's solution (pH=6.5; involving 0.137 M NaCl, 5.4 mM KCl, 0.25 mM Na_2HPO_4, 0.44 mM KH_2PO_4, 1.3 mM $CaCl_2$, 1.0 mM $MgSO_4$, and 4.2 mM $NaHCO_3$). The specimens served as the working electrode for the EC measurement and the reference electrode was a standard Ag/AgCl.

3. Results and discussion

3.1. The basic measurements of the SLM samples

Firstly, the size, appearance, density, and porosity of the resulting SLM solid samples were characterized. The most important item is the index of artifact porosity, because this index will affect appreciably the mechanical and chemical responses of the samples. The average sample density is firstly measured to 4.30 ± 0.1 g/cm^3, only slightly lower than that of the cast Ti-6Al-4V bulk sample (4.43 g/cm^3). The calculated average artifact porosity level is thus $3\% \pm 0.3\%$, compared well with published results [12]. This artifact hole level is considered to be acceptable. This indirectly implies that the setting SLM parameters are suitable and it can be accepted to do the following experiment.

3.2. The SEM/EDS and XRD analyses

The raw Ti-6Al-4V powders, the as-fabricated SLM samples, and the reference rolled plate, were all checked by SEM/EDS for confirming chemical composition before and after SLM. After multiple EDS measurements over larger areas, we found that the composition, though slightly scattered, is basically fixed for all samples under examination, with the average composition within 90.3 ± 0.4 Ti (in wt%), 6.0 ± 0.1 Al, and 3.7 ± 0.3 V. No apparent composition change after SLM.

The Ti-6Al-4V powders are presented in Fig. 2(a), showing highly spherical shape, suitable for SLM process. The powder sizes follows well with the Gaussian size distribution, as shown in Fig. 2(b). The SEM micrographs showing the typical fine needle α′ martensite morphology in the Ti-6Al-4V powders and SLM solid samples are presented in Fig. 2(c) and (d). The predominant fine needle α′ martensite morphology is consistent with the XRD results.

Fig. 3 shows the XRD diffraction pattern of as-received Ti-6Al-4V powders, SLM samples examined from X-, Y- and Z-planes, and the reference rolled plate. According to Fig. 3(a), it is evident that the as-received Ti-6Al-4V powders and the SLM samples (independent of X-, Y-, or Z-plane) contain predominantly the α-phase with the hexagonal closed-packed (HCP) structure, consistent with some previous studies [13–15]. The body centered cubic (BCC) β-phase was not clearly detected for either the as-received powders or the SLM solid samples. If present, the β-Ti phase peaks should appear at 2θ=39.5° and 2θ=57° for the (110) and (200) reflections [16]. This happening is thought to be a result from the high cooling rate during the powder spraying process and the SLM routines. If there were BCC β grains at high temperatures, those β grains would all transform into the HCP α or martensitic α′ phase via the rapid solidification during the SLM process [17]. The SLM processed samples maintain the original composition and crystal structure of the powders.

Furthermore, it can be noted that the XRD peaks in Fig. 3(a) for the HCP Ti-6Al-4V powders and SLM samples all represent the peaks for
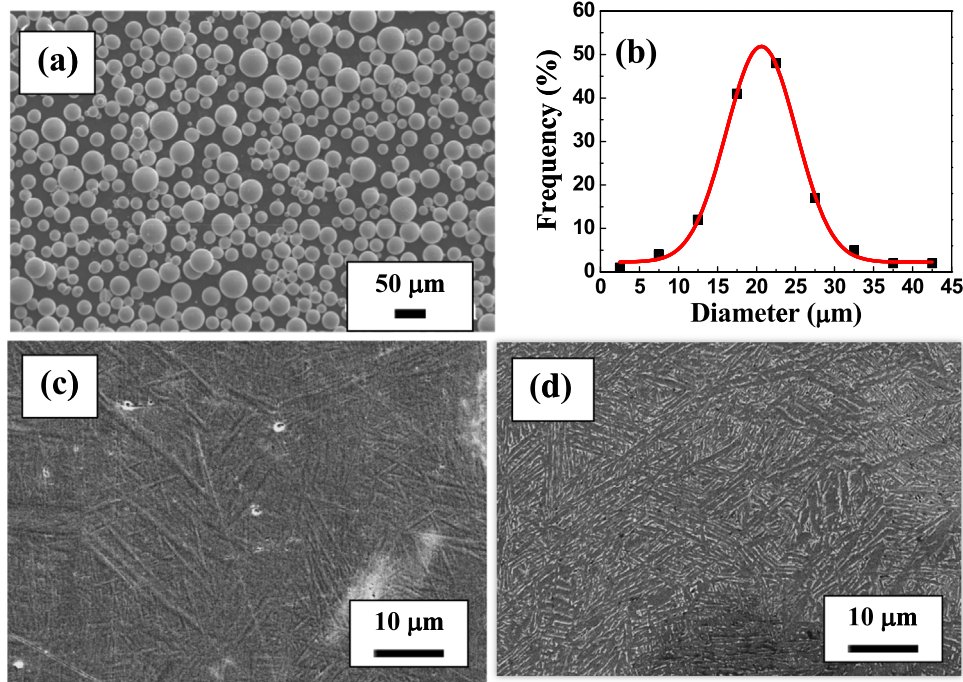
Fig. 2. SEM micrographs showing (a) the spherical Ti-6Al-4V powders, (b) the Gaussian size distribution, and the typical fine needle α' martensite morphology in the Ti-6Al-4V alloy under the (c) as-received powder condition, and (d) SLM sample condition.

randomly distributed orientation with no dominant texture. Such a random grain orientation of the SLM samples is distinctly different from the strong (0002) planar texture observed for the commercial rolled plate shown in Fig. 3(b).

3.3. Mechanical properties

Careful multiple nanoindentation measurements on the X-, Y- and Z-planes of the SLM solid samples were conducted in order to extract the modulus and hardness on these three planes. The average Young's modulus data for all three planes are basically the same, namely, X-plane: 127 ± 2 GPa, Y-plane: 128 ± 2 GPa, and Z-plane: 127 ± 4 GPa, as tabulated in Table 1. These results can be attributed to the similar atomic bonding of the Ti-6Al-4V atoms on the X-, Y- or Z-planes of the SLM products. Modulus data can only be affected by the mutual atomic bonding, not grain shape, grain size or lattice defects. However, the average hardness readings in Table 1 show variation, X-plane: 4.2 ± 0.5 GPa, Y-plane: 5.1 ± 0.5 GPa, and Z-plane: 5.1 ± 0.5 GPa. Similar results were also reported before [18,19]. The hardness measured from the X-plane is consistently lower by 20%, which is appreciable. Since the hardness (and thus the yield and tensile/compression strength)

Table 1

The mechanical properties of as-fabricated SLM processed samples on three different planes. All of the planes (X-plane, Y-plane and Z-plane) are having the nearly same Young's modulus, but the hardness of the X-plane apparently lower. Because using zigzag path strategy will let both Y-plane and Z-plane have whole laser melting path. It means that they have stranger binding than the X-plane.

	X-plane	Y-plane	Z-plane	Rolled plate
Elastic modulus E (GPa)	127 ± 2	128 ± 2	127 ± 4	124 ± 4
HardnessH (GPa)	4.2 ± 0.5	5.1 ± 0.5	5.1 ± 0.5	5.0 ± 0.2

would be affected by material microstructure such as grain shape, grain size, SLM voids or lattice defects, the much lower hardness on the X-plane is a signal that there should have more processing defects on this plane.

Using zigzag back and forth path strategy on the Z-plane will let both Y- and Z-planes have whole laser melting path, as discussed below. However, the X-planes are built during discontinuous laser melting path which would sometimes induce some processing defects to weaken the local hardness or strength. It means that the powders would have stronger binding on the Y- and Z-planes than the powders
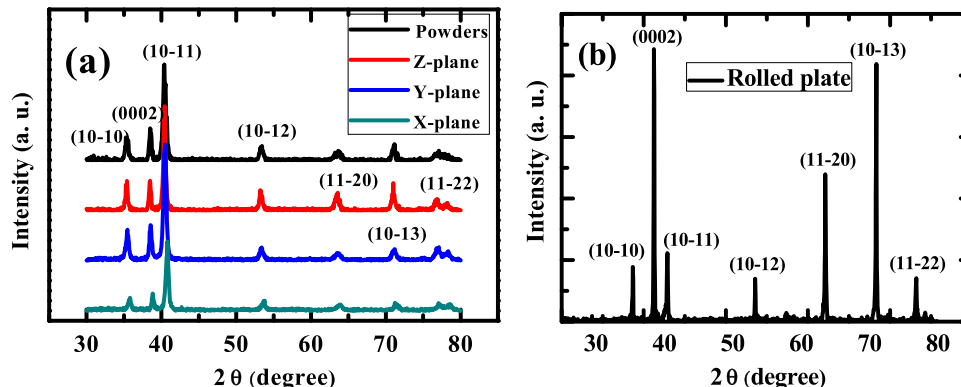

Fig. 3. XRD curves of (a) the as-received Ti-6Al-4V powders, SLM processed Ti-6Al-4V samples, and (b) the commercial cast and rolled Ti-6Al-4V plate. Basically, the as-received powders, as well as the SLM samples along the three different X-, Y- and Z-planes, all have the similar crystal structure, with predominantly the HCP α or α' phase.
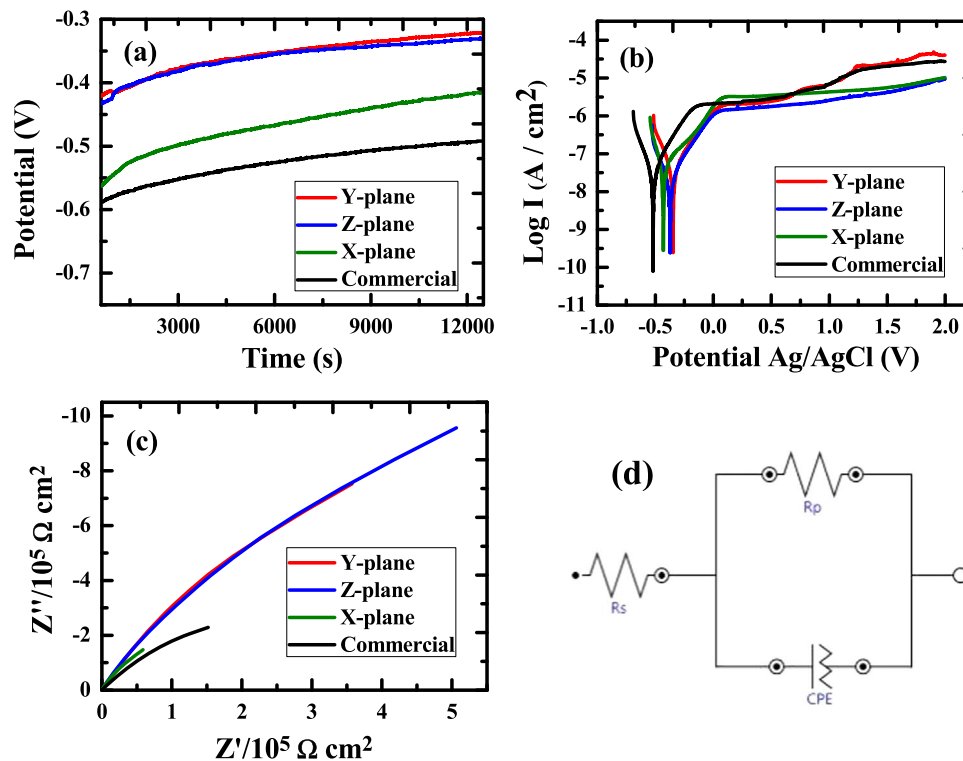
Fig. 4. (a) Open circuit potentials as a function of immersion time of the X-plane, Y-plane and Z-plane SLM processed sample and rolled commercial Ti-6Al-4V plate in SBF at 37 °C. It is found that the analyte and surrounding were more and more stable. (b) Potential polarization curves of the X-plane, Y-plane and Z-plane SLM processed sample and rolled commercial Ti-6Al-4V plate in SBF at 37 °C. (c) The Nyquist plot showing the EIS spectra of the X-plane, Y-plane and Z-plane SLM processed samples and rolled commercial Ti-6Al-4V plate in SBF at 37 °C. (d) The equivalent circuit model of Ti alloys bulk, e.g. Ti-6Al-4V.

Table 2

The electrochemical parameters, E_{corr}, i_{corr}, E_{pit} and i_{pass}, obtain from the potentiodynamic polarization curves of the SLM processed samples with three different sides, and the commercial rolled plate. From E_{corr}, the Y-plane and Z-plane need higher energy to activate the corrosion than the Z-plane. Also, from i_{corr}, it is found that the Y-plane and Z-plane have lower corrosion rate than the Z-plane. It is all because that the X-plane would possess much more artificial porosity during SLM. Those holes will make the EC responses more sensitive. But none of these Ti-6Al-4V samples show severe pitting.

	X-plane	Y-plane	Z-plane	Rolled plate
E_{corr} (V)	−0.48 ± 0.04	−0.33 ± 0.04	−0.36 ± 0.01	−0.52 ± 0.01
E_{pit} (V)	> 2	>2	>2	>2
$\Delta E = E_{pit} - E_{corr}$ (V)	> 2	>2	>2	>2
i_{corr} (10^{-6}A/cm^2)	0.030 ± 0.01	0.023 ± 0.01	0.023 ± 0.01	0.030 ± 0.01
i_{pass} (10^{-5}A/cm^2)	0.482 ± 0.07	0.354 ± 0.05	0.380 ± 0.22	1.362 ± 0.003
R_p (MΩ cm^2)	0.5 ± 0.2	1.3 ± 0.2	1.3 ± 0.1	0.7 ± 0.3

on the X-plane, resulting in higher hardness performance.

3.4. Electrochemical open circuit potential (OCP) analyses

The purpose of the OCP EC response model (also called the E-t curve) is to check the analyte and surrounding being stable or not [20,21]. The SLM samples with the exposed X-, Y- and Z-planes, and the commercial rolled plate, are all immersed in SBF for 12,500 seconds to fully induce the oxidation reaction on the surface. The OCP response of the SLM Y- and Z-planes are basically the same, as shown in Fig. 4(a), reaching saturated at about −0.325 V. But the OCP saturated voltage for the SLM X-plane sample and the commercial rolled plate is −0.415 V and −0.492 V, respectively, meaning the surface oxide layer would form at a lower applied voltage for these samples. The commercial rolled plate appears to possess more rolling defects and residual stress, and would react to form oxide layer more easily. Though the saturated voltages for these four cases are slightly different, they all become saturated and stable, suggesting all these

samples can form protective oxide layer on the surface. By XPS characterization, the formed surface layer is TiO$_2$.

3.5. Electrochemical polarization Tafel curves

There are many corrosion parameters that can be interpreted in the polarization curve, for example, corrosion potential (E_{corr}), corrosion current density (i_{corr}), the potential of pitting (E_{pit}) and the current of passive state (i_{pass}). Each corrosion parameters have its own significance to judge the ability of corrosion resistance. E_{corr} evaluates the energy of corrosion reaction and it is a kind of thermodynamics parameter. i_{corr} evaluates the velocity of corrosion reaction rate and it is a kind of kinetics parameter. E_{pit} decides the easiness of pitting phenomenon and i_{pass} decides the difficulty of oxidation reaction [22,23]. Fig. 4(b) shows that the potentiodynamic polarization curves of SLM and commercial rolled plate samples in SBF at 37 °C. The data on E_{corr}, E_{pit}, i_{corr}, and i_{pass} are listed in Table 2.

It can be seen that the corrosion behavior of the SLM Y-plane and Z-plane samples is again similar (−0.33 and −0.36 V), but is slightly different from that of the SLM X-plane sample (−0.48 V) and the commercial rolled plate (−0.52 V). The E_{corr} data suggest that the commercial rolled Ti-6Al-4V plate needs the least energy (−0.52 V) and will be the first to react, followed by the SLM X-plane sample (−0.48 V).

As for the pitting potential, E_{pit}, and the stable potential interval before pitting, $\Delta E = E_{pit} - E_{corr}$, since we did not find any pitting over the polarization Tafel tests up to 2 V, these four samples are rated to be the same, all exhibiting strong pitting resistance up to 2 V. These Ti-6Al-4V samples all did not exhibit any unwanted pitting reaction.

Besides, the i_{corr} data indicate that commercial rolled Ti-6Al-4V plate and the SLM X-plane sample exhibit a faster reaction rate or a higher corrosion current density (both about 0.030×10^{-6} A/cm^2) than the SLM Y-plane or Z-plane samples (both about 0.023×10^{-6} A/cm^2). The i_{pass} data reflect the similar trend.
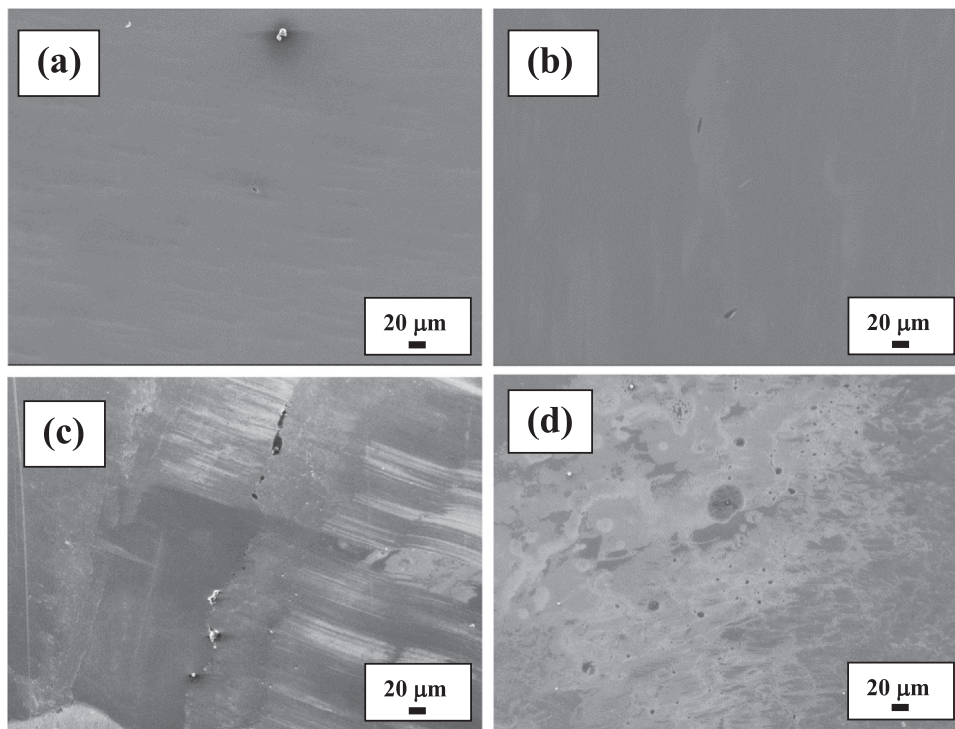
Fig. 5. SEM morographs showing the holes on the (a) Y-plane, (b) Z-plane, and (c)(d) X-plane. The Y- and Z-planes in the SLM sample surfaces tend to be smoother with only few tiny holes widely spased, while th X-plane would show rougher surfaces with much more holes.

Based on the above Tafel and OCP results, the SLM Y-plane and Z-plane samples possess the best bio-corrosion resistance, better than the SLM X-plane sample and even better than the commercial rolled plate. And there exhibits an interesting electrochemical anisotropic response among the X-, Y- and Z-planes.

3.6. Electrochemical A.C. EIS impedance

One general electrochemical impedance method, A.C. impedance, is performed to ensure the above finding. It takes the so-called Nyquist plot to illustrate the electrochemical impedance spectra (EIS) for evaluating the polarization resistance (R_p) [24]. In recent research, it is knows that, if the arc radius of the curve in Nyquist plot is greater, R_p is greater, and the ability of corrosion resistance is better [20]. Fig. 4(c) shows the fitted date via the Nyquist plot for the rolled commercial Ti-6Al-4V sample and SLM processed samples with X-plane, Y-plane and Z-plane. In this A.C. impedance testing, the SLM processed samples with different scanning directions sides (Y-plane and Z-plane) are again showing the similar larger radius, much greater than that of the SLM X-plane sample. In addition, the arc radius of the rolled commercial Ti-6Al-4V sample is also smaller than all of the SLM processed samples. By utilizing the Nyquist and Bode plots, the electrolyte resistance (R_s) and polarization resistance (R_p) of electrochemical impedance spectra (EIS) can be determined. The curves of the Nyquist plot were fit by the equivalent circuit model, $R_s.(CPE-R_p)$. The impedance constant phase element (CPE) is defined as $Z_{CPE}=1/[Q(J\omega)^n]$, where ω is angular frequency, Q is a pre-factor of CPE, and n is its exponent with the range $0 \le n \le 1$. The R_p values determined are also listed in Table 2, where it can be seen that polarization resistance R_p is ~0.5 and ~0.7 MΩ cm² for the X-plane sample and commercial rolled plate, much weaker than that of the Y-plane and Z-plane samples (both ~1.3 MΩ cm²).

Besides, the equivalent circuit model of Ti alloys for fitting the curve of the Nyquist plot in Hank's solution gives a note that the oxide-layer structure (i.e., TiO₂) for the current Ti alloy is a single layer and does not form a three dimensional structure. This single layer TiO₂ oxide

appears to be quite compact, with strong pitting resistance. The equivalent circuit model for the Ti alloys, e.g., Ti-6Al-4V, is shown in Fig. 4(d).

To sum up, the SLM processed Ti-6Al-4V samples, no matter for the X-, Y- or Z-plane, have a better corrosion resistance than the commercial rolled Ti-6Al-4V plate which possesses more rolling defects. By closer comparison, the Y- and Z-planes of the SLM processed samples show a better corrosion resistance than the X-plane.

3.7. The microstructure observations

The common influential factors for EC responses of conventional cast or wrought alloys include (1) alloy chemical compositions, (2) phases, grain sizes and microstructures, and (3) surface conditions [25,26]. It has been reported [27] that there was tiny difference in microstructure viewed from different sample planes of the SLM Ti-6Al-4V samples, and such tiny difference could play critical influence on subsequent corrosion behavior under more severe corrosive environments. The solution system used previously (1 M HCl and 3.5 wt% NaCl) [27] is harsher than the Hank's SBF solution adopted in this study. In our work, the very minor difference in SLM microstructure viewed from various planes did not seem to be the main cause in influencing the subsequent corrosion response of SLM processed Ti-6Al-4V in Hank's SBF. We found that the surface condition (namely, the surface defects on different sample planes which are subject to chemical corrosion contact) of the SLM samples is in fact the prime cause. In this study, it is consistently found that the X-plane has exhibited different (more apparently, worse) responses as compared with the other two Y- and Z-planes. The average hardness H is lower by 20%, the corrosion potential E_{corr} is lower (more prone to initiate surface oxidation), the corrosion current density i_{corr} is higher (more extensive corrosion activity), and the polarization resistance R_p is lower.

The surface conditions were more carefully examined. Fig. 5(a) to (d) present the representative surface morphologies of the Y-plane in Fig. 5(a) and Z-plane Fig. 5(b), as well as the X-plane in Fig. 5(c) and
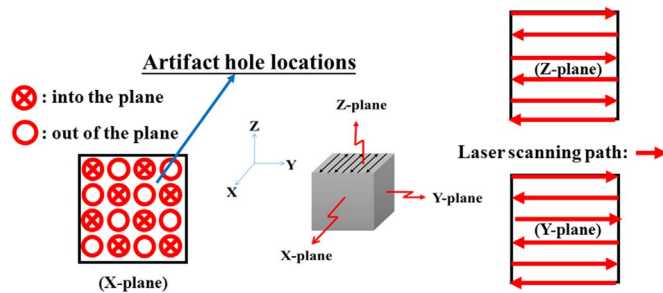
Fig. 6. The holes retained on the X-plane are in much greater density than those on the Y-plane and Z-plane. On the Z- and Y-planes, the laser scanning path is back and forth, and the laser melting is more complete. But the X-plane contains some powder areas with laser path going into the plane and other powder areas with laser coming out of the plane. Holes are easier to form positions between these two areas, where the laser melting is not as complete.
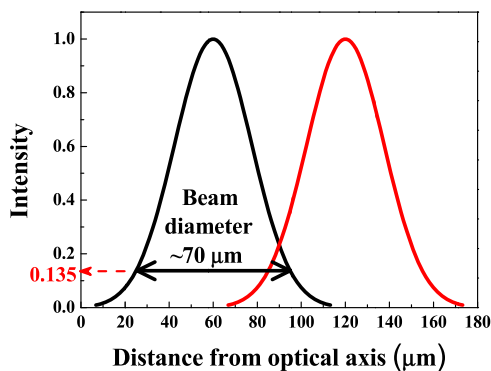

Fig. 7. Intensity distribution of the laser in use. The laser beam size with intensity of 13.5% and above is ~70 µm, and beam size with intensity of 0% and above is ~120 µm. The beam shift distance for each neighboring path is ~60 µm, making the overlap between two neighboring beam paths is estimated to be about 40 µm.

(d). It is clear that the Y- and Z-planes in Fig. 5(a) and (b) reveal quite smooth surface, with only few artifact holes, typically measuring about a few micrometers. These holes were retained by the incomplete SLM melting. In comparison, the X-plane shown in Fig. 5(c) and (d) possesses much higher surface roughness reading, with much higher density such artifact holes by a factor of more than 10.

It is well known that corrosion would initiate from such artifact holes during the OPC, Tafel, and EIS impedance tests. This phenomenon is postulated to be related to the zigzag scanning path strategy the schematic diagram, as shown in Fig. 6. On the right side of this diagram, the laser scanning paths on the Z-plane and Y-plane are both running back and forth. Fig. 7 illustrates the relationship between the laser beam size, ~70 µm (for intensity above 13.5%) and ~120 µm (for intensity above 0%), and the relative overlap, ~40 µm, between neighboring paths. Because of this 40 µm overlap between neighboring paths, the Ti-6Al-4V powders can be basically fully melted on the Z-plane and Y-plane when the laser beam is continuously and smoothly advancing, leaving very few tiny holes, as presented in Fig. 5(a) to (b). In contrast, the laser path on the X-plane, which is the cross-sectional plane with respect to the travelling laser beam, would run into or out of the plane between neighboring paths. The locations in-between the inward and outward paths would be prone to retaining holes. This is because that these locations on the X-plane would encounter discontinuous changes of laser beam direction. The powder melting on such discontinuous and un-smooth laser heating would be more easily induced artifact holes, which phenomena have been widely observed in Fig. 5(c) and (d).

Based on the above findings, those cross-sectional planes of the SLM samples would be easier to be inherent with powder melting artifacts. This effect will lead to an anisotropy effect on the X-plane in terms of lower hardness and lower corrosion resistance.

4. Conclusions

Based on the microstructure and corrosion studies of the SLM Ti-6Al-4V solid samples, the following conclusions can be made.

1. According to the SEM and XRD results, the chemical composition and the orientation texture before and after the SLM procedure are basically the same. The raw material powders were prepared by gas spraying and cooled at very high cooling rates. During SLM, the powders have experienced again the similar heating and cooling history.
2. The Young's modulus of SLM processed X-plane, Y-plane and Z-plane samples are the same. But the hardness reading of the X-plane sample is lower than those of the Y-plane and Z-plane samples by about 20%.
3. The as-fabricated SLM processed X-plane, Y-plane and Z-plane samples all exhibit good electrochemical properties. But by closer comparison, it is consistently found from the electrochemical polarization Tafel curves and the EIS R_p impedance that the X-plane sample shows a lower corrosion resistance than the Y-plane and Z-plane samples. It is because that the X-plane tends to possess more artifact holes induced during SLM with the zigzag laser scanning strategy.

References

[1] I. Gibson, D.W. Rosen, B. Stucker, Additive Manufacturing Technologies, Springer, 2010.
[2] C.N. Elias, M.A. Meyers, R.Z. Valiev, S.N. Monteiro, J. Mater. Res. Technol. 2 (2013) 340–350.
[3] S. Zhang, Q. Wei, L. Cheng, S. Li, Y. Shi, Effects of scan line spacing on pore characteristics and mechanical properties of porous Ti6Al4V implants fabricated by selective laser melting, Mater. Des. 63 (2014) 185–193.
[4] Y. Luo, L. Yang, M. Tian, Application of biomedical-grade titnium alloys in trabecular bone and artificial joints, Biomater. Med. Tribol. (2013) 181.
[5] F. Wang, S. Williams, P. Colegrove, A. Antonysamy, Microstructure and mechanical properties of wire and arc additive manufactured Ti-6Al-4V, Metall. Mater. Trans. A 44 (2013) 968–977.
[6] L.C. Zhang, H. Attar, Selective laser melting of titanium alloys and titanium matrix composites for biomedical applications: a review, Adv. Eng. Mater. 18 (2016) 463–475.
[7] D. Wang, S. Mai, D. Xiao, Y. Yang, Surface quality of the curved overhanging structure manufactured from 316-L stainless steel by SLM, Int. J. Adv. Manuf. Technol. (2015) 1–12.
[8] Y. Lu, S. Wu, Y. Gan, S. Zhang, S. Guo, J. Lin, J. Lin, Microstructure, mechanical property and metal release of As-SLM CoCrW alloy under different solution treatment conditions, J. Mech. Behav. Biomed. Mater. 55 (2015) 179–190.
[9] L. Facchini, E. Magalini, P. Robotti, A. Molinari, S. Höges, K. Wissenbach, Ductility of a Ti-6Al-4V alloy produced by selective laser melting of prealloyed powders, Rapid Prototyp. J. 16 (2010) 450–459.
[10] L. Thijs, F. Verhaeghe, T. Craeghs, J.V. Humbeeck, J.P. Kruth, A study of the microstructural evolution during selective laser melting of Ti-6Al-4V, Acta Mater. 58 (2010) 3303–3312.
[11] C.L. Wang, Y.H. Lai, J.C. Huang, T.G. Nieh, Creep of nanocrystalline nickel: a direct comparison between uniaxial and nanoindentaion creep, Scripta Mater. 62 (2010) 175–178.
[12] H.J. Gong, K. Rafi, H.F. Gu, G.D.J. Ram, T. Starr, B. Stucker, Influence of defects on mechanical properties of Ti-6Al-4V components produced by selective laser melting and electron beam melting, Mater. Des. 86 (2015) 545–554.
[13] Y. Zhou, S.F. Wen, B. Song, X. Zhou, Q. Teng, Q.S. Wei, Y.S. Shi, A novel titanium alloy manufactured by selective laser melting: microstructure, high temperature oxidation resistance, Mater. Des. 89 (2016) 1199–1204.
[14] F. Bartolomeu, S. Faria, O. Carvalho, E. Pinto, N. Alves, F.S. Silva, G. Miranda, Predictive models for physcial and mechanical properties of Ti6Al4V produced by selective laser melting, Mater. Sci. Eng. A 663 (2016) 181–192.
[15] H. Attar, M. Calin, L.C. Zhang, S. Scudino, J. Eckert, Manufacture by selective laser melting and mechanical behavior of commercially pure titanium, Mater. Sci. Eng. A 593 (2014) 170–177.

[16] S.L.R. Da Silva, L.O. Kerber, L. Amaral, C.A. Dos Santos, X-ray diffraction measurements of plasma-nitrided Ti-6Al-4V, Surf. Coat. Technol. 116–119 (1999) 342–346.

[17] J. Yang, H. Yu, J. Yin, M. Gao, Z. Wang, X. Zeng, Formation and control of martensite in Ti-6Al-4V alloy produced by selective laser melting, Mater. Des. 108 (2016) 308–318.

[18] C. Qiu, N.J.E. Adkins, M.M. Attallah, Microstructure and tensile properties of selectively laser-melted and of HIPed laser-melted Ti–6Al–4V, Mater. Sci. Eng. A 578 (2013) 230–239.

[19] W.E. Frazier, Metal additive manufacturing: a review, J. Mater. Eng. Perform. 23 (2014) 1917–1928.

[20] M.P. Pujad, Carbon Nanotubes as Platforms For Biosensors With Electrochemical And Electronic Transduction, Springer, 2012.

[21] P.T. Kissinger, W.R. Heineman, Cyclic voltammetry, J. Chem. Educ. 60 (1983) 702–706.

[22] Y. Tan, Heterogeneous Electrode Processes And Localized Corrosion, Wiley, 2013.

[23] B.R. Barnard, P.K. Liaw, R.A. Buchanan, O.N. Senkov, D.B. Miracle, Oxidation behavior of Ca-based bulk amorphous materials, Mater. Trans. 48 (2007) 1870–1878.

[24] S.M. Park, J.S. Yoo, Electrochemical impedance spectroscopy for better electro-chemical measurements, Anal. Chem. 75 (2003) 455A–461A.

[25] M. Hoseini, A. Shahryari, S. Omanovic, J.A. Szpunar, Comparative effect of grain size and texture on the corrosion behavior of commercially pure titanium processed by equal channel angular pressing, Corros. Sci. 51 (2009) 3064–3067.

[26] N. Dai, L.C. Zhang, J. Zhang, Q. Chen, M. Wu, Corrosion behavior of selective laser melted Ti-6Al-4V alloy in NaCl solution, Corros. Sci. 102 (2016) 484–489.

[27] N. Dai, L.C. Zhang, J. Zhang, X. Zhang, Q. Ni, Y. Chen, M. Wu, C. Yang, Distinction in corrosion resistance of selective laser melted Ti-6Al-4V alloy on different planes, Corros. Sci. 111 (2016) 703–710.